Magnetoacoustic Attenuation, Open Orbits, and Magnetic Breakdown*

PAUL R. SIEVERT†‡
Department of Physics and Institute for the Study of Metals, University of Chicago, Chicago, Illinois
(Received 23 March 1967)

A theory of the magnetic-field dependence of the ultrasonic attenuation in metals is given for some simple models of the Fermi surface. These models exhibit open orbits and allow for magnetic breakdown from open to closed orbits. The theory is semiclassical and is based on a generalization of the path-integral method of solving Boltzmann's equation. Results of calculation are given for magnetic fields perpendicular to the sound wave vector **q**, with both longitudinal and transverse polarizations and with open orbits both parallel and perpendicular to **q**. These cases include the geometry corresponding to the open-orbit resonance observed experimentally in cadmium by Gavenda and Deaton. It is found that (a) the transverse polarization shows open-orbit *antiresonances*; (b) experimental evidence of magnetic breakdown can be obtained only by a detailed examination of the whole line shape; (c) quantum-mechanical coherence effects should manifest themselves as an extra set of highly nonsinusoidal oscillations.

I. INTRODUCTION

AN open-orbit resonance was first observed by Gavenda and Deaton[1] in ultrasonic attenuation measurements made on metallic cadmium [hexagonal close-packed (hcp) structure] in the presence of a magnetic field. The open orbit observed is parallel to the [0001] direction in **k** space. It results from the presence of an energy gap in the ALH plane of the Brillouin zone (B.Z.) which is due to the spin-orbit interaction. The fact that this energy gap exists in all hcp metals was pointed out by Falicov and Cohen,[2] who estimated the gap for magnesium to be 7.5×10^{-6} eV. The gap in cadmium is presumably larger by about two orders of magnitude, yet still small.

For metals with small gaps magnetic breakdown, i.e., magnetic-field induced tunneling of electrons through the gap, has been observed and its effect on the galvanomagnetic properties calculated.[3,4] A small gap Δ means in this context that the condition[5]

$$K\Delta^2/\epsilon_F{}^0\hbar\omega\lesssim 1 \tag{1.1}$$

is satisfied for readily obtainable magnetic fields H; in (1.1) $\epsilon_F{}^0$ is the unperturbed Fermi energy, $\omega=|e|H/mc$ is the cyclotron frequency, m is the free electron mass, and K is a numerical factor of order unity. Complete magnetic breakdown across the spin-orbit induced gap in cadmium would result in closed orbits, i.e., complete disappearance of the open-orbit resonance. Changes of topology of this kind due to magnetic breakdown have drastic effects on the galvanomagnetic properties in general, and the magnetoresistance in particular. It should be pointed out that when magnetic breakdown is almost complete the partial absence of breakdown across the gap introduces an extra scattering mechanism which scatters the electron off of the closed orbit. In the case of the galvanomagnetic tensors, this can be described in terms of an additional effective relaxation time.[3]

It is the purpose of this paper to present a more general procedure for including magnetic breakdown in the theory of transport phenomena in the semiclassical regime. This method is applied to calculate the magnetoacoustic attenuation for a simple model of a metal exhibiting open orbits which have the possibility of breaking down to closed orbits. The line shape of the open-orbit resonance is studied in detail. The previously unanswered question of what constitutes evidence for magnetic breakdown in the magnetoacoustic attenuation[1] receives an answer.

Section II contains the theory relevant to the calculations: Sec. II A is a brief summary of the semiclassical model which is the basis of this work; Sec. II B is a brief statement of the breakdown probabilities that are used; Sec. II C contains the details of the path integral or kinetic method of including magnetic breakdown in the semiclassical transport problem; in Sec. II D the attenuation coefficients are derived in a general way and discussed. The mathematical details of the evaluation of the conductivities and other quantities needed for the calculation of the attenuation coefficients are relegated to an Appendix. Section III contains a description of the models studied and the results of the calculations. Some of the models are chosen so as to exhibit an open-orbit resonance similar in character to that observed in cadmium. In all cases both longitudinal and transverse wave attenuations are calculated. The numerical results of the calculations are also discussed and interpreted; Sec. III A contains a discussion of the results (both numerical and analytic) obtained for closed orbits; Sec. III B contains the presentation and discussion of

* Supported in part by the Advanced Research Projects Agency and the National Science Foundation.
† Submitted in partial fulfillment of the requirements for the Ph.D. degree at the University of Chicago.
‡ Present address: Battelle Memorial Institute, Columbus Laboratories Columbus, Ohio.
[1] J. D. Gavenda and B. C. Deaton, Phys. Rev. Letters 8, 208 (1962); B. C. Deaton and J. D. Gavenda, Phys. Rev. 136, A1096 (1964).
[2] L. M. Falicov and M. H. Cohen, Phys. Rev. 130, 92 (1963).
[3] L. M. Falicov and P. R. Sievert, Phys. Rev. 138, A88 (1965) and the reference quoted therein.
[4] A. B. Pippard, Proc. Roy. Soc. (London) A270, 1 (1962); A256, 317 (1964); A287, 165 (1965); L. M. Falicov, A. B. Pippard, and P. R. Sievert, Phys. Rev. 151, 498 (1966).
[5] See for instance R. W. Stark and L. M. Falicov, in *Progress in Low Temperature Physics*, edited by C. J. Gortor (North-Holland Publishing Company, Amsterdam, to be published), Vol. 5.

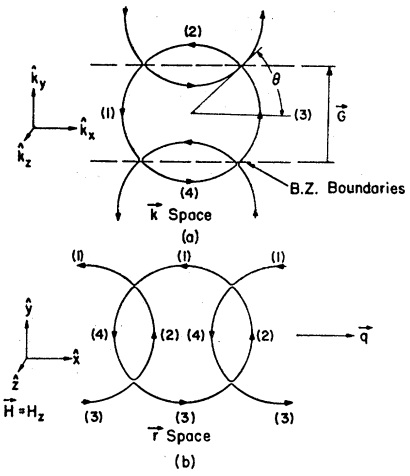

FIG. 1.(a) A Fermi surface in the extended-zone scheme which for no breakdown has open orbits parallel to k_y in the first band and a closed electron piece in the second band. For complete breakdown the surface is a closed circular electron piece. The angle θ measures the amount of Fermi cylinder that contributes to the open orbit, $\sin\theta=|\mathbf{G}|/2k_0$. (b) The corresponding orbits in real space with the direction of the sound propagation vector $\mathbf{q}$ and the external magnetic field $\mathbf{H}$ are shown. The open orbits in real space are parallel to $\mathbf{q}$.

the numerical results for open orbits with no magnetic breakdown operating; Sec. III C is a detailed study of the open-orbit resonance and the effects of the relaxation time and magnetic breakdown; also, the numerical results and a discussion of the effects of magnetic breakdown on the line shape in general are given; Sec. III D presents the results of including quantum oscillations in the breakdown probabilities as given in Sec. II B. Finally, Sec. IV contains a summary of all of the conclusions drawn from the results of these calculations.

II. THEORY

A. General Model

A semiclassical approach to the theory of the magnetoacoustic effect has been shown by Cohen, Harrison, and Harrison[6] (CHH) to be adequate for explaining experimental results in the range of magnetic fields of interest here, i.e., that range corresponding to geometric resonances. A modification of their method is used in this paper. It is assumed that the sound wave can be represented by a velocity field $\mathbf{u}(\mathbf{r},t)\propto\exp[i(\mathbf{q}\cdot\mathbf{r}-\omega_s t)]$. The sound wave has a propagation vector $\mathbf{q}$ and frequency ω_s, dispersion being neglected at this stage. The electrons, N_0 per unit volume, are considered to be "classical" particles which obey a dispersion law $\epsilon(\mathbf{k})$ and Fermi-Dirac statistics. It is also assumed that the pseudopotential at the Fermi level is small enough so that distortion of the Fermi surface due to deformation potential effects can be neglected. In this sense our model is free-electron-like.

Since the electrons are considered classical particles, it is possible to define an electronic distribution function $f=f_0+g(\mathbf{r},\mathbf{k},t)$ which obeys Boltzmann's equation

$$\frac{\partial f}{\partial t}+\mathbf{v}\cdot\frac{\partial f}{\partial \mathbf{r}}+\frac{\mathbf{F}}{\hbar}\cdot\frac{\partial f}{\partial \mathbf{k}}=\left(\frac{\partial f}{\partial t}\right)_{\text{coll}}. \tag{2.1}$$

In (2.1), we have

$$\mathbf{F}=\hbar(d\mathbf{k}/dt)=-|e|(\mathbf{E}+(\mathbf{v}/c)\times\mathbf{H}), \tag{2.2}$$

and

$$\mathbf{v}=(1/\hbar)\partial\epsilon(\mathbf{k})/\partial\mathbf{k}. \tag{2.3}$$

Further, f_0 is the unperturbed Fermi-Dirac distribution, $\mathbf{k}$ is the propagation vector describing the state (i.e., position of the electron in $\mathbf{k}$ space), $\mathbf{E}$ is an internal electric field set up by the sound wave, and $\mathbf{H}$ is the external magnetic field. (The magnetic field set up by the sound wave is small compared to the external field and is therefore neglected.) A relaxation time ansatz

$$\partial f/\partial t|_{\text{coll}}=-(f-f_s)/\tau \tag{2.4}$$

is made; in (2.4) it is assumed that the electrons scatter into the local equilibrium distribution

$$f_s(\mathbf{r},\mathbf{k},t)=f_0(\mathbf{k}-m\mathbf{u}/\tau,\epsilon_F(\mathbf{r},t)), \tag{2.5}$$

and τ is assumed constant everywhere on the Fermi surface. Expanding to first order in $\mathbf{u}$ and quantities proportional to $\mathbf{u}$, we obtain the solution of the above Boltzmann equation in terms of Chamber's path integral[6,7]

$$g(\mathbf{r},\mathbf{k},t)=-(\partial f_0/\partial\epsilon)[\mathbf{J}(\mathbf{k})\cdot(\mathbf{E}-m\mathbf{u}/\tau)+(\epsilon_F{}^0/N_0\tau)K(\mathbf{k})N_1], \tag{2.6}$$

where

$$(\mathbf{J}(\mathbf{k}),K(\mathbf{k}))=\int_{-\infty}^{t(\mathbf{k})}(-|e|\mathbf{v}(t'),1)\times\exp\{i[\mathbf{q}\cdot(\mathbf{r}(t')-\mathbf{r}(t))-\omega_s(t'-t)]-(t-t')/\tau\}dt' \tag{2.7}$$

and the time t' parametrizes the path followed by the electron in $\mathbf{k}$ space previous to the time t. Equation (2.7) is called the path integral.

It is now assumed that the Fermi surface is a circular cylinder of height Δk_z and radius k_0 so that $d\epsilon/dN=\epsilon_F{}^0/N_0$. The problem is thus reduced to two dimensions, which makes the resonances sharper but does not essentially alter the physical situation in spite of the considerable deviation from a free-electron sphere. This is so because we consider only cases where $\mathbf{q}\perp\mathbf{H}$ and $\mathbf{H}$ is parallel to the cylinder axis. At very low temperature we have $\partial f_0/\partial\epsilon\simeq-\delta(\epsilon-\epsilon_F{}^0)$ and consequently only electrons at the Fermi surface contribute to the trans-

[6] M. H. Cohen, M. J. Harrison, and W. A. Harrison, Phys. Rev. 117, 937 (1960).

[7] R. G. Chambers, Proc. Phys. Soc. (London) A65, 458 (1952); A238, 344 (1956).

port phenomena; moreover, electrons on the Fermi surface "cylinder" circulate perpendicularly to **H**, as seen from the solution of (2.2) and (2.3) for **E**=0.

B. Magnetic Breakdown

If there were no periodic lattice potential or if k_0 were such that the entire Fermi surface cylinder was contained within the first BZ, the electrons would have circular paths in **k** space. However, when the lattice potential is nonvanishing and k_0 is larger than some dimension of the first BZ, Bragg reflection takes place and the electronic paths become more complicated. For example, Fig. 1 depicts a Fermi surface and BZ boundaries such that there is an open orbit parallel to the x axis in real space (which is also parallel to $\mathbf{q}=q\hat{x}$) when there is no magnetic breakdown. Using the labels of the pieces of the cylinder in Fig. 1(a), with no magnetic breakdown the electrons follow the paths 1–1–1–1 and 3–3–3–3 for open orbits and 2–4–2–4 for the closed electron orbit. When magnetic breakdown is complete the electron follows the circular closed electron orbits 1–4–3–2–1. For partial breakdown the paths are not uniquely defined and they form a network on which the electrons describe a random walk. In other words, an electron on 1 has a probability P of having arrived there after tunneling from 2, and a probability $Q=1-P$ of having arrived directly from 1. The tunneling probability P is given by[8]

$$P=\exp(-H_0/H), \tag{2.8}$$

where

$$H_0=K\Delta^2 mc/\epsilon_F{}^0 he. \tag{2.9}$$

Here $\epsilon_F{}^0$ is the Fermi energy, Δ is the energy gap, and K is a constant of order unity. As shown in Fig. 1(a), the angle θ measures the amount of Fermi cylinder that contributes to the open orbit, so that $\sin\theta=|\mathbf{G}|/2k_0$, where **G** is the reciprocal lattice vector. In the case when θ approaches $\frac{1}{2}\pi$ it is seen that the Fermi cylinder has in fact only two, instead of four, pieces (see Fig. 2), and the probabilities P and Q are replaced by[3]

$$S=2Q/(1+Q) \tag{2.10}$$

and

$$T=P(1+Q)=1-S. \tag{2.11}$$

In these equations, S is the probability of following the Bragg reflected path and T is the tunneling (free electron) probability; P is given by (2.8). If θ is so close to $\frac{1}{2}\pi$ that the electron piece is small enough to be in the oscillatory regime,[4] the quantum-mechanical phase coherence of the electrons on this piece must be accounted for. This results in

$$S=2Q(1-\cos\phi)/(1+Q^2-2Q\cos\phi) \tag{2.12}$$

and

$$T=P^2/(1+Q^2-2Q\cos\phi)=1-S, \tag{2.13}$$

[8] M, H, Cohen and L. M. Falicov, Phys. Rev. Letters 7, 231 (1961); E. I. Blount, Phys. Rev. **126**, 1636 (1962).

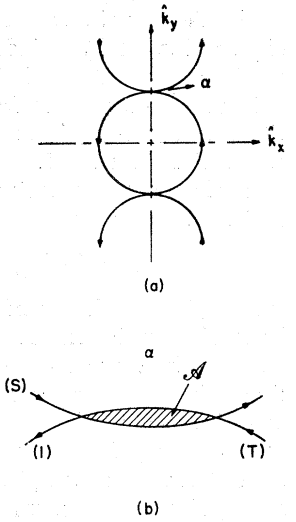

FIG. 2.(a) The Fermi surface in the extended-zone scheme corresponding to that of Fig. 1(a), with θ very close to $\frac{1}{2}\pi$. (b) Detail of the small electron piece whose position is indicated by α in Fig. 2(a) and where the tunneling probabilities mentioned in the text are shown.

where T, S, P, and Q have the same meaning as above and where

$$\phi=(hc\mathfrak{A}/eH)-\phi_0. \tag{2.14}$$

In (2.14), $\mathfrak{A}$ is the area of the vanishingly small electron piece in **k** space, and ϕ_0 is a constant phase. In all calculations, the "rounding off" of the Fermi surface due to the lattice potential in the vicinity of the junctions is neglected.

C. The Path Integral

The path integral, Eq. (2.7), is now used to include magnetic breakdown into the solution of the transport problem. Because time t parametrizes the position of the electron on its phase-space path and since all our models are two dimensional, only the time dependence of the path integral is made explicit in what follows. Equation (2.7) can be written

$$\begin{aligned}(\mathbf{J}(t),K(t))=\int_{t_0}^{t}&(-|e|\mathbf{v}(t'),1)\\ &\times\exp\{i[\mathbf{q}\cdot(\mathbf{r}(t')-\mathbf{r}(t))-\omega_s(t'-t)]-(t-t')/\tau\}dt'\\ &+\exp\{i[\mathbf{q}\cdot(\mathbf{r}(t_0)-\mathbf{r}(t))-\omega_s(t_0-t)]-(t-t_0)/\tau\}\\ &\times(\mathbf{J}(t_0),K(t_0)).\end{aligned} \tag{2.15}$$

The path integral for the time t is thus broken up into contributions from the times between t_0 and t plus the path integral for t_0 modified by a weight factor. As seen in (2.15), this weight factor, the coefficient of $(\mathbf{J}(t_0), K(t_0))$, has a phase associated with a change of position of the electron with time relative to the sound wave. The magnitude of the coefficient is associated with the scattering of electrons off the path between points corresponding to times t_0 and t. The above formulation of the path integral can be used in the way described below.

The Fermi cylinder is divided into a finite number n of pieces labeled by an index l running from 1 to n. This would correspond physically to the way in which the BZ boundaries cut the free-electron Fermi sphere (or the Fermi cylinder in our two-dimensional model). A conduction electron circulates on the Fermi surface in each piece with its position in $\mathbf{k}$ space related to its position in $\mathbf{r}$ space by

$$\hbar\mathbf{k}=(-|e|/c)[(\mathbf{r}-\mathbf{r}_0)\times\mathbf{H}], \tag{2.16}$$

where $\mathbf{r}_0$ is an arbitrary origin. The individual pieces can be considered simultaneously, i.e., a different time variable can be defined for each piece. Suppose that the time origin $t=0$ for the lth piece is taken at the time at which the transit of that piece begins, and t_l is the corresponding time at which the transit is completed. An electron in the lth piece can be followed back from some point corresponding to t, to the beginning of the piece corresponding to the time origin for that piece. Then it can be said to have come from the end of some other piece p corresponding to t_p for the time variable in that piece. As can be seen from (2.15), the path integral depends only on the relative position $\mathbf{r}(t)-\mathbf{r}(t')$ and the time difference $t-t'$, the velocity being given by (2.3) as just the local energy gradient on the Fermi surface. So if the position and velocity in the lth piece are denoted by $\mathbf{r}(l,t)$ and $\mathbf{v}(l,t)$, respectively, the path integral for a time t at which the electron is in the lth piece can be given by a reformulation of (2.15) setting $t_0=0$. This is

$$(\mathbf{J}(l,t),K(l,t))=(\mathbf{I}(l,t),I_0(l,t)) +D(l,t)(\mathbf{J}(p,t_p),K(p,t_p)), \tag{2.17}$$

where $(\mathbf{J}(p,t_0),K(p,t_p))$ is the path integral for the end of the pth piece corresponding to t_p and where

$$(\mathbf{I}(l,t),I_0(l,t))=\int_0^t (-|e|\mathbf{v}(l,t),1) \times\exp\{i[\mathbf{q}\cdot(\mathbf{r}(l,t')-\mathbf{r}(l,t))-\omega_s(t'-t)] -(t-t')/\tau\}dt', \tag{2.18}$$

$$D(l,t)=\exp\left\{-i[\mathbf{q}\cdot\Delta\mathbf{r}(l,t)-\omega_s t]-\frac{t}{\tau}\right\}, \tag{2.19}$$

and

$$\Delta\mathbf{r}(l,t)=\mathbf{r}(l,t)-\mathbf{r}(l,0). \tag{2.20}$$

Since (2.17) governs the contribution of $(\mathbf{J}(p,t_p),K(p,t_p))$ to $(\mathbf{J}(l,t),K(l,t))$ through $D(l,t)$, magnetic breakdown can be included as an additional weight factor which gives the probability of connecting various pieces of Fermi surface. Using the breakdown probabilities defined above we have, in general,

$$(\mathbf{J}(l,t),K(l,t))=(\mathbf{I}(l,t),I_0(l,t)) +D(l,t)\sum_{p=1}^{n} M_{lp}(\mathbf{J}(p,t_p),K(p,t_p)), \tag{2.21}$$

where M_{lp} (the $n\times n$ breakdown matrix of Ref. 3) is the probability that an electron in the piece l has come from the piece p. In the example in Fig. 1 for some general θ, M_{lp} is

$$\mathbf{M}=\begin{bmatrix} Q & P & 0 & 0 \\ 0 & 0 & P & Q \\ 0 & 0 & Q & P \\ P & Q & 0 & 0 \end{bmatrix}. \tag{2.22}$$

If we let $\mathbf{q}$ and ω_s tend to zero to obtain the uniform static case, Eq. (2.21) still represents a generalization of previous methods used to include magnetic breakdown effects in the calculation of galvanomagnetic tensors.[3,4]

The method of obtaining the solution of (2.21) for the path integrals is to set $t=t_l$ and solve the resulting set of simultaneous linear equations. Then these solutions are inserted back into (2.21) for arbitrary t. The total electronic current can now be written following CHH,[6] as

$$\mathbf{j}_e=\boldsymbol{\sigma}\cdot(\mathbf{E}-m\mathbf{u}/e\tau)-\mathbf{R}N_1|e|v_s, \tag{2.23}$$

where, for the two dimensional models calculated here,

$$\sigma_{ij}=\frac{-|e|m\omega}{4\pi^2\hbar^2}\Delta k_z\sum_{l=1}^{n}\int_0^{t_l} v_i(l,t)J_j(l,t)dt \tag{2.24}$$

and

$$R_i=\frac{\epsilon_F{}^0 m\omega}{4\pi^3 N_0\tau v_s}\Delta k_z\sum_{l=1}^{n}\int_0^{t_l} v_i(l.t)K(l,t)dt. \tag{2.25}$$

Here ω is the cyclotron frequency, m is the free-electron mass, and v_s is the velocity of sound. Also in this two-dimensional scheme the equilibrium electron density is $N_0=k_0\Delta k_z/4\pi^2$, where Δk_z is the height of the Fermi cylinder. Note that

$$i\mathbf{q}\cdot\mathbf{I}(l,t)=-|e|\{1-[(1-i\omega_s\tau)/\tau]I_0(l,t)-D(l,t)\} \tag{2.26}$$

which is obtained by an integration by parts on t' in (6.18). Using (2.26) and the fact that

$$\sum_{p=1}^{n} M_{lp}=1$$

because of conservation of probabilities, it is easily shown that

$$i\mathbf{I}(l,t)\cdot\mathbf{q}=-|e|\{1-[(1-i\omega_s\tau)/\tau]K(l,t)\} \tag{2.27}$$

and consequently for $\mathbf{q}=q\hat{x}$,

$$R_i=\frac{-i\omega_s\tau(v_F/v_s)^2}{2(1-i\omega_s\tau)}\frac{\sigma_{i1}}{\sigma_0}. \tag{2.28}$$

Thus the discussion of Eq. (2.16) in CHH [which is identical to (2.27)] goes through here unchanged. The conductivity tensor $\boldsymbol{\sigma}$ and the diffusion vector $\mathbf{R}$ are now used in the formulation of the attenuation coefficient.

D. Attenuation Coefficient

The wave equation for sound propagating in the x direction in a metal is[9]

$$\partial^2\mathbf{S}/\partial t^2-v_s^2\partial^2\mathbf{S}/\partial x^2=\mathbf{F}/N_0M\,, \tag{2.29}$$

where M is the ionic mass, $\mathbf{F}$ is the force acting on the ions as described below, N_0 is the ionic density (assumed to be the same as the electron density), v_s is the velocity of sound before interactions with the conduction electrons are included, and $\mathbf{S}$ is the ionic displacement field. By assuming the velocity field of the sound wave to have the dependence

$$\mathbf{u}(\mathbf{r},t)\propto\exp\{i[(q+iA)x-\omega_s t]\}\,,$$

we have $\mathbf{S}=i\mathbf{u}/\omega_s$, and (2.29) becomes

$$[-i\omega_s+i(v_s^2/\omega_s)(q+iA)^2]\mathbf{u}=\mathbf{F}/N_0M\,. \tag{2.30}$$

Here iA is the deviation of the wave number from $q=\omega_s/v_s$ induced by interaction with the electrons; A may be regarded as a complex amplitude attenuation coefficient. The force $\mathbf{F}$ is given by

$$\mathbf{F}=N_0|e|(\mathbf{E}+(\mathbf{u}/c)\times\mathbf{H})+\mathbf{F}_c\,, \tag{2.31}$$

where $\mathbf{E}$ is the self-consistent electric field, $\mathbf{H}$ is the external magnetic field (the internal magnetic field is neglected), and $\mathbf{F}_c$ is the coherent force which feeds energy coherently back into the ion system. The coeherent force is due to the electron-ion collisions and has the form[6]

$$\mathbf{F}_c=(N_0m/\tau)(\langle\mathbf{v}_e\rangle-\mathbf{u})\,, \tag{2.32}$$

where $\langle\mathbf{v}_e\rangle$ is the average electronic velocity. The forces due to the deformation potential are neglected. The average electronic velocity is given by

$$\langle\mathbf{v}_e\rangle=-\mathbf{j}_e/N_0|e| \tag{2.33}$$

in terms of the electronic current $\mathbf{j}_e$; and the total current $\mathbf{j}$,

$$\mathbf{j}=\mathbf{j}_e+N_0|e|\mathbf{u}\,, \tag{2.34}$$

is related to the self-consistent field $\mathbf{E}$ by Maxwell's equations as given in CHH

$$\mathbf{j}=-\sigma_0\mathbf{B}\cdot\mathbf{E}\,; \tag{2.35}$$

for $\mathbf{H}=H\hat{z}$ and $\mathbf{q}=q\hat{x}$ we have

$$\mathbf{B}=\begin{pmatrix}-i\gamma & 0\\ 0 & i\beta\end{pmatrix}, \tag{2.36}$$

where

$$\beta=\omega c^2/4\pi\sigma_0 v_s^2 \tag{2.37}$$

and

$$\gamma=\beta(v_s/c)^2 \tag{2.38}$$

Here β is the screening parameter and is proportional to the square of the ratio of the classical skin depth to the sound wavelength, typically of order 10^{-5} for metals of interest. σ_0 is the dc conductivity. Solving for $\mathbf{E}$ as in CHH we obtain

$$\mathbf{E}=(N_0e/\sigma_0)\mathbf{W}\cdot\mathbf{u}\,, \tag{2.39}$$

where

$$\mathbf{W}=-(\boldsymbol{\sigma}'+\mathbf{B})^{-1}\cdot(\mathbf{I}-\boldsymbol{\sigma}')\,, \tag{2.40}$$

$$\boldsymbol{\sigma}'=(\mathbf{I}-\mathbf{R})^{-1}\cdot\boldsymbol{\sigma}/\sigma_0\,, \tag{2.41}$$

and

$$R_{ij}=R_i\delta_{1j}\,. \tag{2.42}$$

The form of the tensor $\boldsymbol{\sigma}'$ and the vector $\mathbf{R}$ results from the constitutive equation, Eq. (2.23) above which reduces to

$$\mathbf{j}_e=\sigma_0\boldsymbol{\sigma}'\cdot(\mathbf{E}-m\mathbf{u}/e\tau)\,, \tag{2.43}$$

when the equation of continuity,

$$(\mathbf{j}_e)_1=-N_1cv_s \tag{2.44}$$

in this case, is used. Using (2.33), (2.35), and (2.39) in (2.31) and (2.32), we obtain the expression for the force

$$\mathbf{F}=-(N_0^2c^2/\sigma_0)\mathbf{S}\cdot\mathbf{u}+(N_0|e|/c)\mathbf{u}\times\mathbf{H}\,, \tag{2.45}$$

where

$$\mathbf{S}=(\mathbf{I}+\mathbf{B})[(\boldsymbol{\sigma}'+\mathbf{B})^{-1}(\mathbf{I}+\mathbf{B})-\mathbf{I}]. \tag{2.46}$$

Inserting this into (2.30) and neglecting terms quadratic in A we obtain

$$A\mathbf{u}=\mathbf{D}\cdot\mathbf{u}\,, \tag{2.47}$$

where

$$\mathbf{D}=\tfrac{1}{2}(mv_F/Mv_s)l^{-1}[\mathbf{S}-\omega\tau\mathbf{G}] \tag{2.48}$$

and

$$\mathbf{G}=\begin{pmatrix}0 & 1\\ -1 & 0\end{pmatrix}. \tag{2.49}$$

The electronic mean free path is given by $l=v_F\tau$. Equation (2.47) is an eigenvalue equation for the complex amplitude attenuation coefficient A. Because $\mathbf{S}$ and $\mathbf{G}$ have off-diagonal terms, the normal modes are mixtures of longitudinal and transverse waves. Solving for the eigenvalues yields

$$A_\pm=\tfrac{1}{2}(D_{11}+D_{22})\pm\tfrac{1}{2}(D_{21}-D_{22})\times\left[1+\frac{4D_{12}D_{21}}{(D_{11}-D_{22})^2}\right]^{1/2}. \tag{2.50}$$

The term $(4D_{12}D_{21})/(D_{11}-D_{22})^2$ in Eq. (2.50), arises from the mode mixing. It was calculated for the case of complete breakdown $P=1$, i.e., for the simple circular electron orbit, and in the case of no breakdown $Q=1$, i.e., when open orbits were present. In both cases both the real and imaginary parts of this term were no greater than 10^{-3} for the magnetic fields of interest. This shows that mode mixing, although detectable for other field orientations,[10,11] is small here and can be neglected. The relative energy attenuations that are calculated are

[9] T. Kjeldaas, Phys. Rev. **113**, 1473 (1959).

[10] B. I. Miller, Phys. Rev. **151**, 519 (1966).

[11] H. P. Aubauer, Phys. Rev. **155**, 673 (1967).

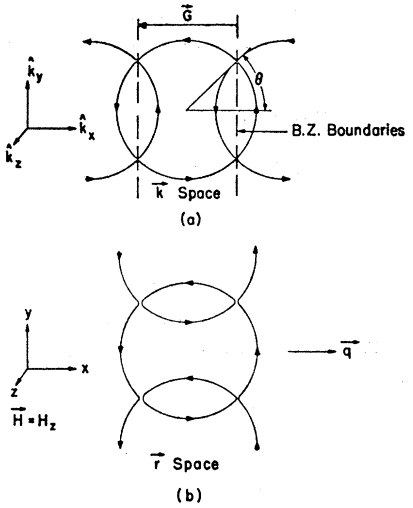

FIG. 3.(a) A Fermi surface in the extended-zone scheme which for no breakdown has open orbits parallel to k_z in the first band and a closed electron piece in the second band. The angle θ here measures the amount of Fermi cylinder that contributes to the closed lens-shaped orbit, $\cos\theta=|\mathbf{G}|/2k_0$. (b) The corresponding orbits in real space with the direction of the sound propagation vector $\mathbf{q}$ and the external magnetic field $\mathbf{H}$ shown. The open rbits in real space are perpendicular to $\mathbf{q}$.

$\mathrm{Re}(S_{11})$ corresponding to the positive sign in (2.50) and to longitudinal waves, and $\mathrm{Re}(S_{22})$ corresponding to the negative signs and to transverse waves. These are given by

$$\mathrm{Re}(S_{ii})=\mathrm{Re}\{(1+B_{ii})^2[(\boldsymbol{\sigma}'+\mathbf{B})^{-1}]_{ii}\}-1, \quad (2.51)$$

which is the same expression used by CHH. [Eq. (2.44) in Ref. 6]. In terms of $\boldsymbol{\sigma}'$ (2.51) becomes

$$\mathrm{Re}(S_{11})=\mathrm{Re}\left\{\frac{\sigma_{22}'+i\beta}{\sigma_{11}'(\sigma_{22}'+i\beta)+(\sigma_{12}')^2}\right\}-1 \quad (2.52)$$

and

$$\mathrm{Re}(S_{22})=\mathrm{Re}\{\sigma_{11}'/[\sigma_{11}'(\sigma_{22}'+i\beta)+(\sigma_{12}')^2]\}-1, \quad (2.53)$$

where we have neglected γ. Also we have used the fact that $\sigma_{21}'=-\sigma_{12}'$ which is a consequence of (2.28) and the relation $\sigma_{12}=-\sigma_{21}$.[12]

The mechanism of the attenuation can be explained in terms of a response argument first given by CHH. The argument is as follows: Since the screening in real metals is almost complete, i.e., β is small, we have a constant current system, i.e., the internal electric field $\mathbf{E}$ which is induced changes in such a way so as to force the electronic current to equal, and cancel the ionic current $Ne\mathbf{u}$; this means that the attenuation, which can be given schematically as

$$\mathrm{Re}(A)\propto\mathrm{Re}(\mathbf{E}\cdot\mathbf{j}_e)-1, \quad (2.54)$$

is proportional to the resistance

$$\mathrm{Re}(A)\propto\mathrm{Re}(\boldsymbol{\varrho}'\cdot\mathbf{j}_e\cdot\mathbf{j}_e)-1. \quad (2.55)$$

The minus one that occurs in (2.55) is due to energy being coherently fed back into the sound wave by the collision drag force $m\mathbf{u}/\tau$. Here $\boldsymbol{\varrho}=[\sigma_0\boldsymbol{\sigma}']^{-1}$, $\boldsymbol{\sigma}'$ measuring the total response to the field, i.e., the diffusion vector has been included. Thus, when β is neglected, the form of the attenuation (2.52) and (2.53) can be understood in this way.

The evaluation of the formulas for the conductivity tensors and diffusion vectors as well as those of the relative attenuation coefficients are quite straightforward but very cumbersome; the procedure is indicated in the Appendix. The numerical results displayed in the figures were obtained using the IBM 7094-7040 complex of the University of Chicago Computation Center.

III. MODEL CALCULATIONS

The Fermi surface models that are used in this calculation are shown in Figs. 1 and 3. They are constructed from pieces of circular cylinder as described above. Also, as mentioned above, we consider only the cases where the magnetic field $\mathbf{H}$ is perpendicular to the sound propagation vector $\mathbf{q}$, so that we always take $\mathbf{H}=H\hat{z}$ and $\mathbf{q}=q\hat{x}$. When there is no magnetic breakdown both Figs. 1 and 3 exhibit open orbits in the x-y plane, Fig. 1 shows open orbits parallel $\mathbf{q}$, whereas Fig. 3 shows open orbits perpendicular $\mathbf{q}$. We shall also, in all cases, confine our attention to that range of magnetic fields and sound frequencies where the phonon wavelength is of the order of the classical orbit radii, i.e., to the range of geometric resonances or geometric oscillations. In this case ω is much greater than ω_s (by a factor v_F/v_s which in our case is taken to be 500). Finally, since we are interested in free-electron-like metals the parameter β is always chosen to be small, i.e., about 10^{-4}.

A. Closed Orbits

Before considering the results for open orbits and magnetic breakdown, we consider simple closed orbits in our two-dimensional model. The results of the numerical calculation of the relative attenuations for closed orbits are given in Figs. 4(a) and 4(b) as functions of $\omega\tau$ for longitudinal and transverse waves, respectively. In this case $ql=40$ and $\beta=8\times10^{-5}$. We can explain these results better by going through an argument similar to that in CHH (Sec. IV of Ref. 6), only here we have no spherical polar angle to integrate over because our model of the Fermi surface is a circular cylinder. By keeping only the $n=0$ and $n=1$ terms in our series, which correspond to Eq. (4.1) of CHH, we

[12] This is always found to be so for the symmetry of the problem here discussed.

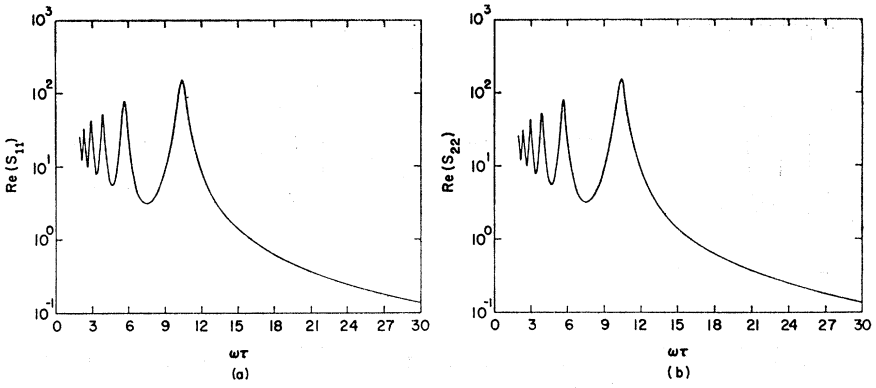

FIG. 4(a). The relative attenuation of longitudinal sound waves for closed orbits corresponding to a cylindrical Fermi surface. The values of the parameters are $v_F/v_s=500$, $ql=40$, and $\beta=8\times10^{-6}$. (b) The corresponding relative attenuation of transverse waves.

obtain

$$\frac{\sigma_{11}}{\sigma_0}\simeq\frac{2(1-i\omega_s\tau)}{q^2l^2}\{1-J_0^2(X)-J_1^2(X)B\},$$

$$\frac{\sigma_{12}}{\sigma_0}=-\frac{\sigma_{21}}{\sigma_0}\simeq\frac{1}{q^2l^2}\{[J_0^2(X)]'+[J_1^2(X)]'B\}, \quad (3.1)$$

$$\frac{\sigma_{22}}{\sigma_0}\simeq\frac{2}{(1-i\omega_s\tau)}\{[(J_0(X))']^2+[(J_1(X))']^2B\}.$$

Here $B=2(1-i\omega_s\tau)/\omega^2\tau^2$, $X=\omega_s v_F/\omega v_s$ is the argument of the Bessel functions, $l=v_F\tau$ is the electronic mean free path, and we have assumed $\omega\gg\omega_s$ and $\omega^2\tau^2\gg1$, which are approximations appropriate to the range of fields where geometric resonances or oscillations are important. The prime in (3.1) denotes differentiation with respect to X. Using the above results in (2.28), (2.42), and (2.53), we obtain

$$\mathrm{Re}(S_{22})\simeq(1-J_0^2(X))/2J_1^2(X)-1 \quad (3.2)$$

for the relative attenuation of transverse sound waves. In (3.2) we have neglected terms containing B, i.e., we have kept only the $n=0$ terms in the series. We note that (3.2) exhibits no explicit dependence on τ and that it increases without limit at fields corresponding to the zeros of $J_1(X)$.

When calculating the longitudinal sound wave attenuation (2.52) in this approximate way it is not meaningful to neglect all terms containing B, since in that case we obtain the nonsensical result $\mathrm{Re}(S_{11})=-1$. When terms linear in B are kept,

$$\mathrm{Re}(S_{11})\simeq X^2([J_1(X)]')^2/J_1^2(X)-1. \quad (3.3)$$

We see that again there is no explicit dependence on τ and that the zeros of $J_1(X)$ give the positions of the maxima. This is in contrast to the results of CHH. In their calculation, with a spherical Fermi surface as a model, they obtain an explicitly τ dependent result by keeping only the $n=0$ terms. The above considerations are a consequence of the two-dimensional model; however, since we are mainly interested in open orbits which occur usually only in narrow bands of the Fermi surface, the model is valid and the essential mechanisms here are correct.

For transverse waves and closed orbits, the response argument given above takes a particularly simple form which can be used to explain (3.2). We review it here because similar arguments are used later. Detailed analysis shows that for transverse waves the only important component of the conductivity tensor is σ_{22}, and of that the real part is predominant; in this way we have

$$\mathrm{Re}(S_{22})\simeq\sigma_0/\mathrm{Re}(\sigma_{22})-1. \quad (3.4)$$

The important contribution is thus due to the response of the electron to a transverse electric field which is essentially a stationary one. The physical stiuation is illustrated in Fig. 5. In case (a) the field is always directed against the electrons' motion; therefore, the electron speed monotonically decreases with each passage. If the orbit were displaced a half-wavelength, the speed would monotonically increase. In both cases there is an increase in the current in phase with the field, which corresponds to a large current response, large real conductivity, and low attenuation. Case (b) shows the electron alternately being accelerated and decelerated by the field in one cycle; therefore, one obtains a small current response, low conductivity, and high attenuation. The orbit radius r in case (b) and in any case of maximum attenuation in the geometric resonance or geometric oscillation[13] range corresponds to the condition

$$X=qr=n\pi, \quad n=1,2,3,\cdots. \quad (3.5)$$

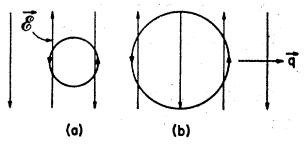

FIG. 5. Closed orbits in real space with a transverse wave schematically represented by the important component of the self-consistent electric field E. Case (a) represents the electron orbit corresponding to high conductivity (low attenuation)· case (b), an electron orbit corresponding to low conductivity (high attenuation).

[13] We shall refer to the attenuation oscillation as geometric oscillations when they are due to closed orbits and geometric resonances when they refer to open orbits.

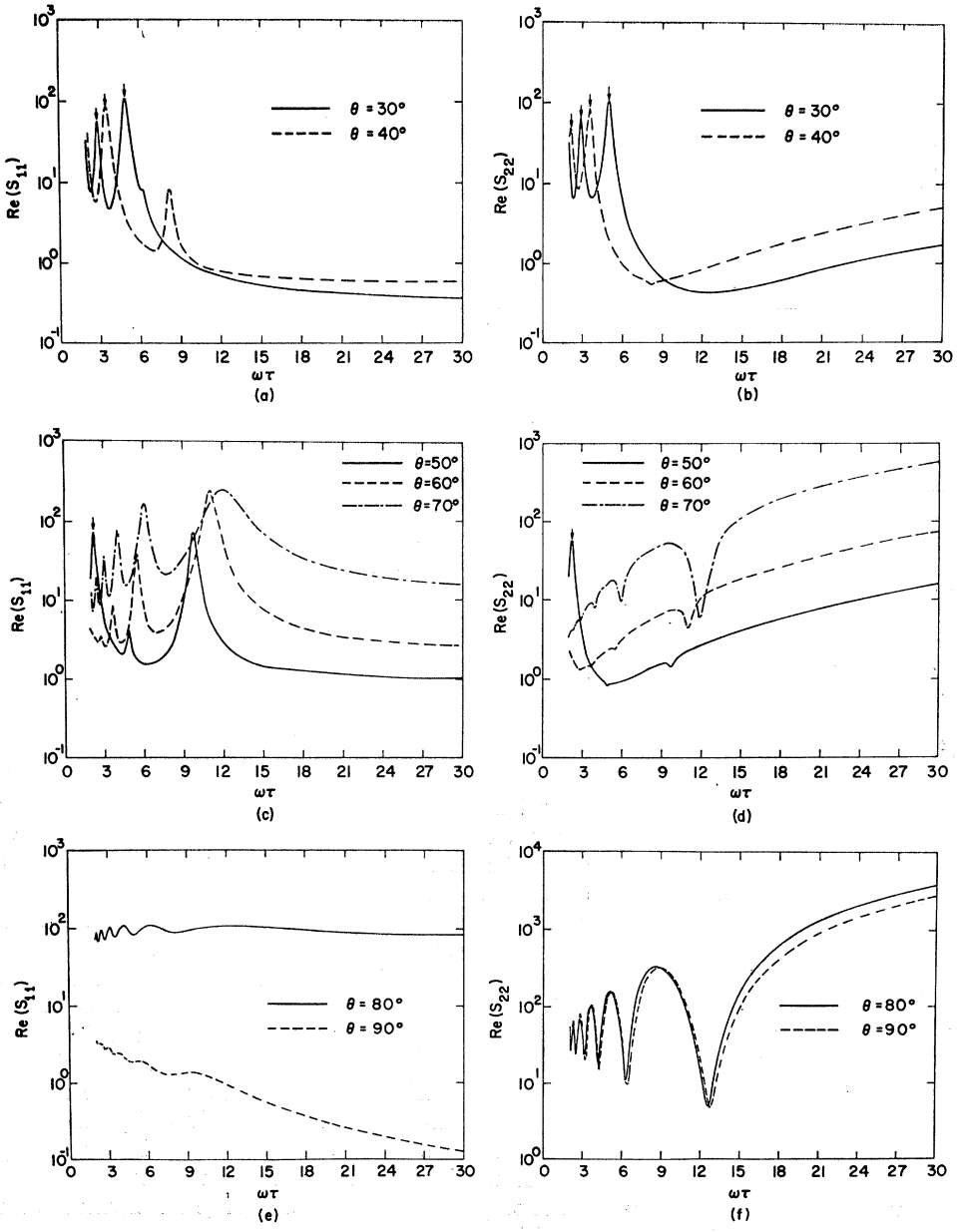

FIG. 6. Relative attenuation for the models shown in Figs. 1 and 2 with no magnetic breakdown and the various θ's indicated. For this case the open orbit in real space is parallel to $\mathbf{q}$. The longitudinal sound wave results are given in (a), (c), and (e) and the corresponding transverse wave results in (b), (d), and (f). The values of the parameters here are $v_F/v_s=500$, $ql=40$, and $\beta=8\times10^{-6}$.

This condition on X corresponds approximately to the zeros of $J_1(X)$ for high magnetic fields, in fact, as the field increases the geometric oscillation peak approaches the field point corresponding to (3.5) from the low side. A study of the conductivities for all cases considered in this paper shows that (3.4) is valid for transverse waves, in general. Simple response arguments like the one above can therefore be used to explain the attenuation of transverse waves in all cases.

The situation, even for closed orbits, is much more complicated when the attenuation of longitudinal waves is considered. In this case the diffusion term contributes strongly, and there is a delicate cancellation of terms in ql. Also, the off-diagonal components of the conductivity tensor are not negligible, so that self-consistent Hall fields are important. The situation becomes so difficult as to prevent the formulation of a simple picture similar to that for transverse waves. However, it can be seen from the similarity of (3.2) and (3.3) that the attenuation peaks for longitudinal waves provide a means of measuring the same sort of calipers of the Fermi surface as do the transverse waves. This is presumably true in general.

B. Open Obrits

The results of the calculation of the attenuation for open orbits are given in Figs. 6 and 7. Figure 6 contains the results for the model shown in Fig. 1 which has the

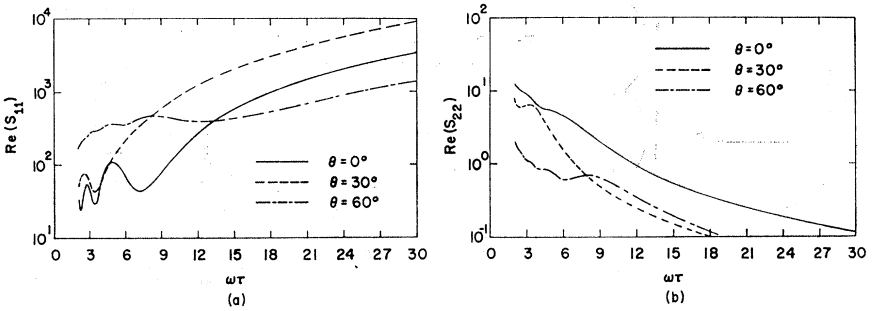

FIG. 7. Relative attenuations for the model shown in Fig. 3 with no magnetic breakdown and the various angles indicated. In this case the open orbit in real space is perpendicular to **q**. The longitudinal sound wave results are given in (a) and the corresponding transverse wave results in (b). The values of the parameters are the same as for the cases in Fig. 6.

open orbit parallel to the same propagation vector **q** in real space and the angle θ measuring the amount of the Fermi cylinder that contributes to the open orbit so that $\sin\theta=|\mathbf{G}|/2k_0$. Figure 7 contains the results for the model shown in Fig. 3 which has open orbits perpendicular to **q** in real space and θ in this case measuring the amount of the Fermi cylinder that contributes to the closed-lens shaped piece of Fermi surface, $\frac{1}{2}\pi-\theta$ contributing to the open orbits, so that $\cos\theta=|\mathbf{G}|/2k_0$. In all these cases $ql=40$ and $\beta=8\times10^{-5}$.

For the case of Fig. 6, (a), (c), and (e) give the results for longitudinal wave attenuation. The geometric resonance occurs when the average value (taken over the period T of the motion which is fixed by the BZ boundaries and the strength of the magnetic field) of the velocity satisfies the condition $\langle\mathbf{v}_e T\rangle_{\text{av}}\cdot\mathbf{q}=2\pi n$, $n=1, 2, \cdots$. In terms of θ this becomes

$$(ql/n\pi)\sin\theta=(\omega\tau)_{\text{res}}. \tag{3.6}$$

Closed-orbit geometric oscillations due to the calipering of the lens piece are also present with the position of the maxima given approximately by

$$(ql/n\pi)(1-\sin\theta)\simeq(\omega\tau)_{\max}. \tag{3.7}$$

Equations (3.7) estimates the field corresponding to the oscillation maxima. The period is given approximately by

$$P(1/\omega\tau)=\pi/ql(1-\sin\theta). \tag{3.8}$$

The resonances are shown in Fig. 6(a), (c), and (e) as θ increases. For small θ, less of the Fermi cylinder goes to the open orbit and the resonances are small. As θ increases they become larger and more frequent [according to (3.6)] until θ approaches 90° when a degeneration in [see Fig. 6(e)]. In the integral involved in the calculation of the conductivities, the end points of the Fermi cylinder segment contribute strongly. These critical points correspond to points in real space where the electronic velocity $\mathbf{v}_e$ has a considerable component parallel to the self-consistent longitudinal electronic field **E** for small θ. The velocity component parallel **E** decreases until for $\theta=90°$ it vanishes. This evidently accounts for the degeneration observed in the results. The geometric oscillations due to the lens are seen in Fig. 6(a) and (c) (marked by arrows at the maxima) and the period is seen to be given by (3.8). Also, these oscillations are smaller in magnitude than those of the simple circular closed orbits of Fig. 4(a) because less of the cylinder contributes in this case.

The transverse wave attenuations for open orbits parallel **q** are given in Fig. 6(b), (d), and (f) for increasing θ. The most striking feature of these results is the emergence of geometric antiresonances corresponding in position to the condition (3.6). These antiresonances are superposed on a general rise with increasing $\omega\tau$ and θ in the attenuation which is due to the average of $(\mathbf{v}_e)_x$ over the period T being large and is just the ordinary open-orbit effect seen in magnetoresistance data. A simple response argument is sufficient to explain these antiresonances. Figure 8 shows the transverse self-consistent electric-field configuration that gives the antiresonance. The important part of the open orbit is the "scallop." It is here where the field is effective in increasing monotonically the electrons velocity, giving a large response or a small attenuation. If the sound wave were displaced half a wavelength, the electronic velocity is monotonically decreased and the same argument holds. For a quarter wavelength displacement, the electron is accelerated and decelerated and there is no effective response. In addition, the deeper the scallop, i.e., the larger θ, the greater the magnitude of the antiresonance, because $\mathbf{v}_e$ is more nearly parallel to **E** for longer segments of the orbit. This effect is seen in the results. Closed-orbit oscillations due to calipering the lens are also seen in Figs. 6(b) and (d); they are similar to the longitudinal attenuation results (marked by arrows in the figure). They can be interpreted in exactly the same way as the circular closed orbits described above. Finally, there is an anomaly in Fig. 6(f): the over-all attenuation for $\theta=90°$ in lower than that for $\theta=80°$, reversing the general trend for other angles. This is undoubtedly a result of using a two-piece Fermi cylinder for the $\theta=90°$ case as illustrated in Fig. 2(a), one piece of the Fermi surface has vanished.

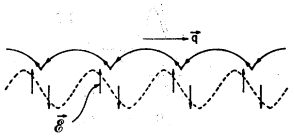

FIG. 8. An open orbit in real space parallel to the sound propagation vector **q** with a transverse wave schematically represented by the important component of the self-consistent electric field **E**. The configuration represents the situation corresponding to antiresonances in the transverse wave relative attenuations.

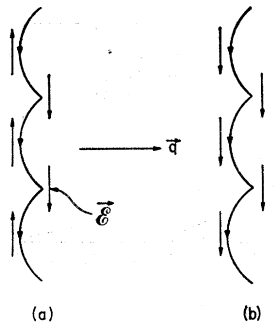

FIG. 9. Open orbits in real space perpendicular to the sound propagation vector **q** with a transverse wave schematically represented by the important component of the self-consistent electric field **E**. The configuration corresponding to the attenuation maxima for transverse sound waves is given in (a) and the attenuation minima in (b).

Figures 7(a) and 7(b) give the results of longitudinal and transverse wave attenuations, respectively, in the case where the open orbits are perpendicular to **q** in real space. There are no pronounced resonances or antiresonances; however, there appears to be some weak structure. In the transverse wave attenuation there are weak maxima [Fig. 7(b), $\theta=0°$, 30°] that correspond to the field configuration and calipering shown in Fig. 9(a). The condition for maxima in this case is

$$(\omega\tau)_{\max}=(ql/2\pi n)(1-\sin\theta),\quad n=1,2,3,\cdots. \tag{3.9}$$

The response argument can again be used to point out that the field shown in Fig. 9(a) accelerates and decelerates the electron in a single period leading therefore to maxima in the attenuation. Figure 9(b) is the situation corresponding to minima in the attenuation, i.e., the electron is monotonically accelerated (or decelerated if the electron-field configuration is displaced a half wavelength) in a single period. This effect is stronger for $\theta=30°$ than for $\theta=0°$ because for the former case the scallop is shallower, so that in the neighborhood of the scallop point the electronic velocity v_e has a larger component parallel to the electric field **E** at the resonance configuration. When condition (3.9) is satisfied

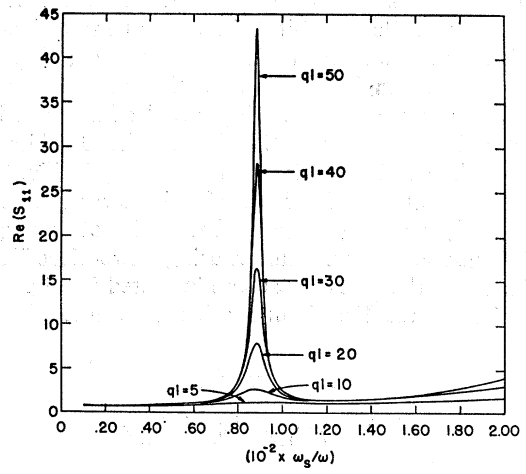

FIG. 10. The details of an open-orbit resonance for longitudinal sound waves. This is the case corresponding to Fig. 1 with $\theta=45°$. The resonance condition $\omega_s/\omega=n\pi/(v_F/v_s)\sin\theta$ reduces in this case to $\omega_s/\omega=0.89\times10^{-2}$. The dependence of the line shape on the electronic mean free path is shown.

the longitudinal waves show attenuations minima for $\theta=0°$ and 30°. The case $\theta=60°$ appears to be degenerated for both longitudinal and transverse waves. However, (3.9) indicates that for this case we would not expect minima or maxima at values of the field in the range under consideration. It should finally be pointed out that the general rise in the attenuations for longitudinal waves [Fig. 7(a)] is due to $\langle(v_e)_y\rangle_{av}$ being large and is thus a consequence of ordinary open-orbit magnetoresistive effect.

C. Magnetic Breakdown of Open Orbits

In this section the effect of magnetic breakdown on the line shape of the attenuations is studied. First, however, Fig. 10 shows the effect of changing the relaxation time (or equivalently ql) on an isolated open orbit resonance. For this case the open orbit is parallel to **q** in real space, $\theta=45°$ and β is negligible, i.e., of order 10^{-4}. The resonance is in the longitudinal wave attenuation and it is at $\omega_s/\omega=0.89\times10^{-2}$ which corresponds to a resonance field $H_r=5.1$ kG. The resonance has a Lorentzian line shape in agreement with the calculation of Kaner, Peschanski, and Privoratski[14] and it has the expected dependence on ql. Both the closed-orbit oscillations and open-orbit resonances exhibit the same kind of dependence on ql. This is another consequence of our two-dimensional model, where all the electrons at a given angular position are in the same phase relation to the sound wave.

The change in line shape when magnetic breakdown occurs is seen in Figs. 11(a) and 11(b). For this case $ql=40$, $\beta=8\times10^{-5}$, (the parameters ql and β have these values for all the rest of the calculations presented in this section) $\theta=45°$, and we take the breakdown or tunneling probability P as given in (2.8). In this case the open orbits parallel to **q** in real space break down to closed orbits. The breakdown parameter H_0 was expressed in terms of $P(H_r)$, the value of the probability P for $H=H_r$. In this case $H_r=5.1$ kG and we have the correspondence

$$\begin{aligned}
&P(H_r)=0 \quad\leftrightarrow H_0=\infty,\\
&P(H_r)=0.005\leftrightarrow H_0=27.000\text{ kG},\\
&P(H_r)=0.050\leftrightarrow H_0=15.299\text{ kG},\\
&P(H_r)=0.300\leftrightarrow H_0=\ 6.136\text{ kG},\\
&P(H_r)=0.700\leftrightarrow H_0=\ 1.831\text{ kG},\\
&P(H_r)=1 \quad\leftrightarrow H_0=0.
\end{aligned}$$

In Fig. 11(a) one sees a maximum at high fields even for small breakdown probabilities. This is due to the averaging of maxima corresponding to the calipers of a number of extended orbits which exist when there is partial breakdown. The magnitude of the resonance

[14] É. A. Kaner, V. G. Peschanskii, and I. A. Privorotski, Zh. Eskperim. i Teor. Fiz. **40**, 214 (1961) [English transl: Soviet Phys.—JETP **13**, 147 (1961)].

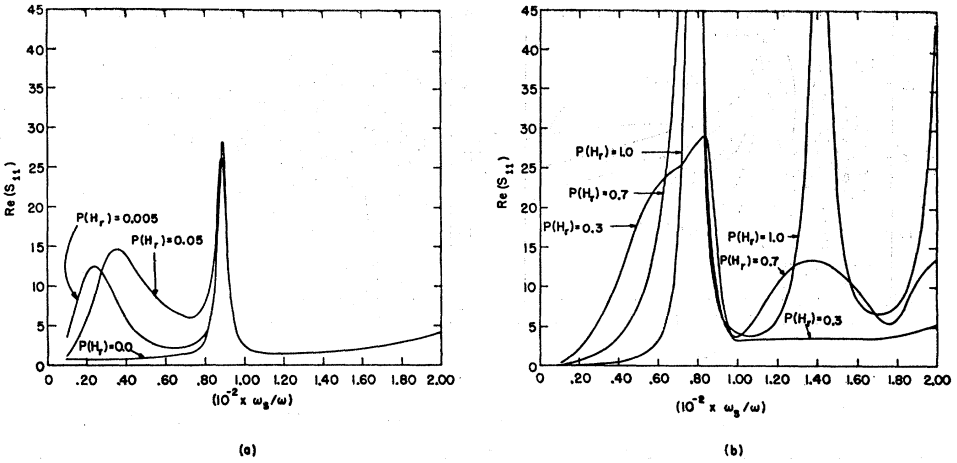

FIG. 11. The effect of magnetic breakdown on the open-orbit resonance of Fig. 10 for $ql=40$: The results are given for various values of the breakdown probability P in (a) and (b). An explanation of the P's is given in Sec. III C.

remains practically unchanged until, as seen in Fig. 11(a), it is "swamped" by what becomes the maximum of the circular closed-orbit oscillation. Other circular closed-orbit oscillation maxima can also be seen to grow as breakdown increases. This result indicates that little evidence of magnetic breakdown can be seen experimentally by a study of the details of the open-orbit resonances alone. The whole line shape must be observed. Since Gavenda and Deaton[1] can still observe a resonance in their experiments, the results in Fig. 11(b) indicate that $P(H_r)<0.3$, so that the breakdown parameter H_0 for the spin-orbit gap in cadmium must be greater than 6 kG. It would be interesting in this respect to repeat the experiment at several sound frequencies and compare the resultant curves. Also, we see from the line shape that theoretically deviation from complete magnetic breakdown cannot be described as an interband scattering with an effective relaxation time for time- and position-dependent transport phenomena. This is in contrast to the simple explanation of the magnetoresistance data.[3,4]

The results for $\theta=45°$, $ql=40$, and $\beta=8\times10^{-5}$ are shown in Fig. 12 over a more extended range of fields and as a function of $\omega\tau$ on a logarithmic scale. The transverse-attenuation results are given in Fig. 12(b) and the limiting curves, i.e., the $H_0=\infty$ and, $H_0=0$ curves are shown. Figure 13 depicts the attenuation results for $\theta=60°$. A number of open-orbit resonances are displayed in Fig. 13(a) and a more pronounced antiresonance is shown in Fig. 13(b). The effects of magnetic breakdown on the line shape can be clearly observed. Figure 14 exhibits the results for the case $\theta=90°$, where for this calculation a two-piece Fermi cylinder and the effective breakdown probabilities (2.10) and (2.11) are used. Figure 14(a) shows the rise of the closed-orbit oscillations from the degenerated open-orbit results. The line shape of the transverse wave attenuation, Fig. 14(b), shows that open-orbit antiresonances are similar in form to the circular closed-orbit oscillations except for being inverted and shifted in position. Magnetic breakdown results in some intermediate line shape. Attenuation results of cases involving magnetic breakdown where the open orbit is perpendicular $\mathbf{q}$ are given in Figs. 15 and 16, $\theta=45°$ and $\theta=0°$, respectively.

All of the preceding results have used breakdown probabilities involving $\exp(-H_0/H)$ only. However, if when magnetic breakdown occurs and a very small piece of the Fermi surface is involved, one cannot neglect quantum-mechanical phase coherence in these small pieces. We show the effect of this phase coherence in the next section.

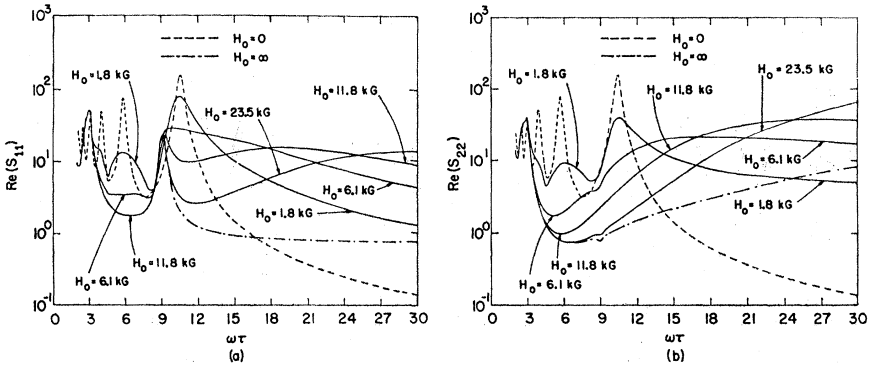

FIG. 12.(a) The longitudinal sound wave attenuation results for an open-orbit resonance undergoing magnetic breakdown in the case corresponding to Fig. 1 for $\theta=45°$; $ql=40$, $v_F/v_s=500$, and $\beta=8\times10^{-5}$; (b) the corresponding results for transverse waves.

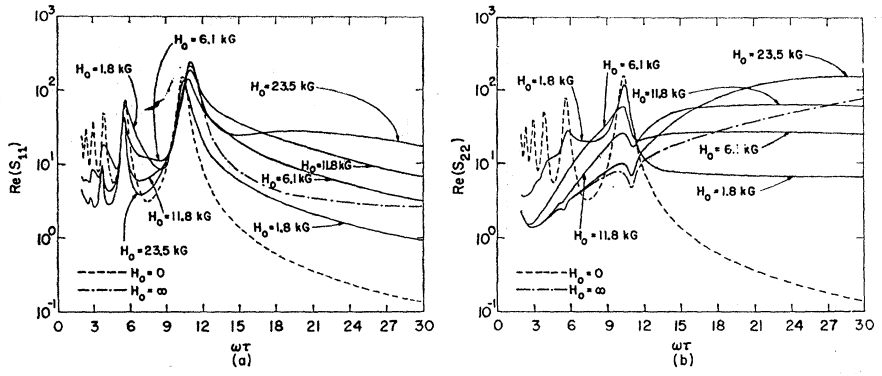

FIG. 13.(a) The longitudinal sound wave attenuation results for open-orbit resonances undergoing magnetic breakdown in the case corresponding to Fig. 1 for $\theta=60°$; $ql=40$, $v_F/v_s=500$, and $\beta=8\times10^{-5}$; (b) the corresponding results for transverse waves. The disappearance of the antiresonance is to be noted.

D. Oscillating Magnetic Breakdown Probabilities

For very small lens pieces, i.e., when θ is very close to 90° for the open-orbit parallel to **q** case, or θ very close to 0° for the open-orbit perpendicular to **q** case, the quantum-mechanical phase coherence of the electrons on the lens must be accounted for in the breakdown probabilities. The oscillating effective probabilities (2.12) and (2.13) are used in the calculation here in conjunction with a two-piece Fermi cylinder, the case of Fig. 2 serving as an example. The phase ϕ can be written $\phi=\omega_1\tau/\omega\tau+\phi_0$ and in the calculation here we take $\phi_0=0$ and a typical value of 200 for $\omega_1\tau$. Also, H_0 is chosen to be 6.14 kG. The results of the calculation are presented by the solid-line curves in Figs. 17(a) and 17(b), which correspond to the open-orbit parallel to **q** case and longitudinal and transverse wave attenuation, respectively. Figures 17(c) and 17(d) show the open-orbit perpendicular to **q** case for longitudinaall and transverse wave attenuations, respectively. In this calculation we take as before $ql=40$, $\beta=8\times10^{-5}$. The results are plotted logarithmically against ω_s/ω. so that the periodicities are more evident and the limiting curves, i.e., the $H_0=0$ or circular closed-orbit attenuation and the $H_0=\infty$ or open-orbit attenuation, are also shown.

The effect of the phase coherence in the small piece is seen to be the introduction of very sharp "spiky" oscillations superposed on the open orbit or $H_0=\infty$ curves. These spikes get sharper as the magnetic field decreases. For $\cos\phi=+1$,

$$S=1 \quad \text{and} \quad T=0, \tag{3.10}$$

whereas for $\cos\phi=-1$ we have

$$S=4Q/(1+Q)^2, \qquad T=((1-Q)/(1+Q))^2. \tag{3.11}$$

From Eqs. (3.10) and (3.11) we can see that the spikes of the oscillations always touch the closed orbit $H_0=0$ curve, no matter what value one has for $\omega_1\tau$ and Φ. The envelope of these oscillations will always be the same as the closed-orbit curve, and this is shown in Fig. 17 to be the case in our calculation here. This feature is only a consequence of the model. The rate at which the spiked curves approach the $H_0=\infty$ curves with decreasing magnetic field depends on H_0: The smaller H_0 the faster the rate of approach. Also, since the spikes must touch the closed-orbit curve for any field value, the smaller H_0 the sharper the spikes become as the magnetic field is decreased. We note here again the open-orbit magnetoresistance effect, i.e., of Figs. 17(a) and 17(b): It is (b) which shows the indefinite increase for high magnetic fields whereas of (c) and (d) it is (c) that shows this effect.

IV. CONCLUSIONS

We summarize the main conclusions to be drawn from this paper as follows:

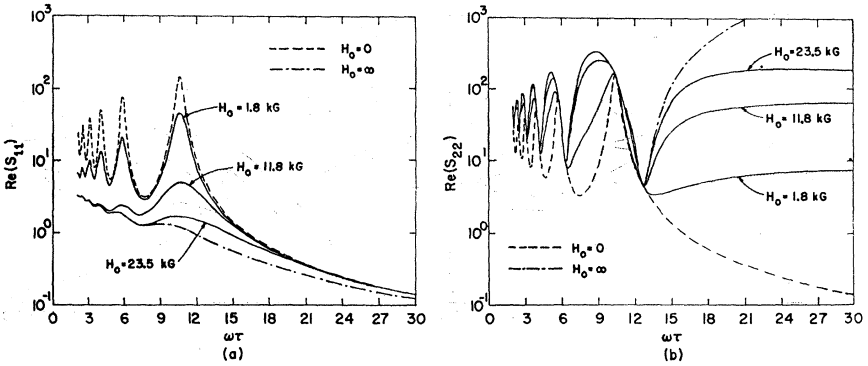

FIG. 14.(a) The longitudinal sound wave attenuation results for open orbits undergoing magnetic breakdown in the case corresponding to Fig. 2, i.e., $\theta=\frac{1}{2}\pi$ so there is no closed lens-shaped piece; (b) the corresponding results for transverse waves.

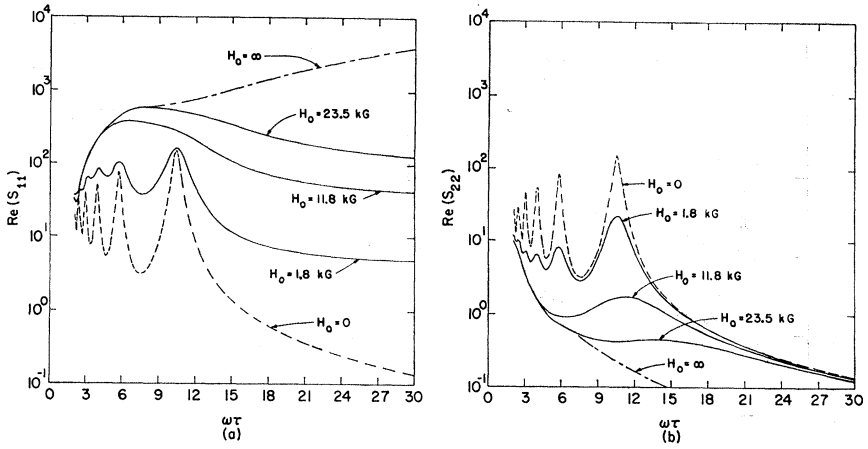

FIG. 15(a) The longitudinal sound wave attenuation results for open orbits undergoing magnetic breakdown in the case corresponding to Fig. 3 for $\theta=45°$, the open orbit in real space is perpendicular to $\mathbf{q}$; (b) the corresponding results for transverse waves.

(a) A study of the conductivity tensor reveals that for transverse waves the only important component is σ_{22} and of that $\mathrm{Re}(\sigma_{22})$ predominantes; therefore, transverse wave attenuation can always be understood simply in terms of the response to the transverse component of the self-consistent electric field. The situation for longitudinal waves is much more complicated because diffusion and off-diagonal components of the conductivity tensor contribute strongly; therefore, it is not possible to understand longitudinal wave attenuation with any simple picture of the response argument. The results indicate, however, that the longitudinal wave attenuation provides calipers of the Fermi surface similar to the transverse wave attenuation.

(b) Open-orbit geometric resonances appear in the longitudinal wave attenuation for a somewhat convoluted open orbit in a normal fashion. The transverse wave attenuation, however, exhibits pronounced geometric antiresonances for this convoluted open-orbit, and these can be simply explained by a response argument.

(c) A study of the details of an open-orbit geometric resonance when varying amounts of magnetic breakdown is taking place indicates that evidence for magnetic breakdown is taking place indicates that evidence for magnetic breakdown can be reliably obtained only in magnetoacoustic-attenuation experiments when the entire line shape over a fairly wide range of magnetic fields is analyzed. This is because magnetic breakdown does not alter the resonance line shape locally; instead, a closed-orbit geometric oscillation due to calipering extended orbits appears at higher magnetic fields.

(d) Finally, it is evident from a comparison of the ql dependence of the open-orbit geometric resonance and the behavior described in (c) above that deviation from complete magnetic breakdown *can not* be understood as an interband scattering describable by an effective relaxation time for any time- and position-dependent transport phenomena.

Note added in proof. It has been pointed out to the author by Dr. E. I. Blount, that in Eq. (2.31) one extra contribution to the force has been omitted. This is an impulsive term responsible, in some electron trajectories, for the Bragg reflection that takes place at well defined points. This term, as far as the author is aware, has not been considered previously in the literature and should produce an effect in the attenuation coefficient.

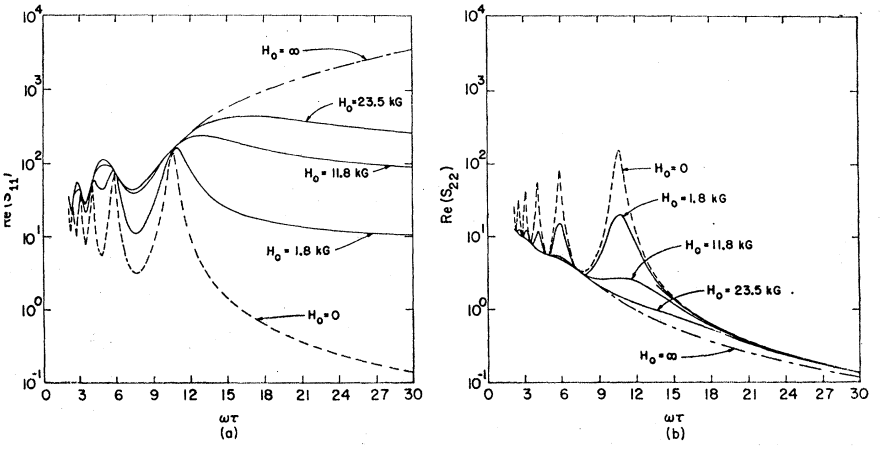

FIG. 16.(a) The longitudinal sound wave attenuation results for open orbits undergoing magnetic breakdown in the case corresponding to Fig. 3 for $\theta=0°$; all other parameters are as in Fig. 13; (b) the corresponding results for transverse waves.

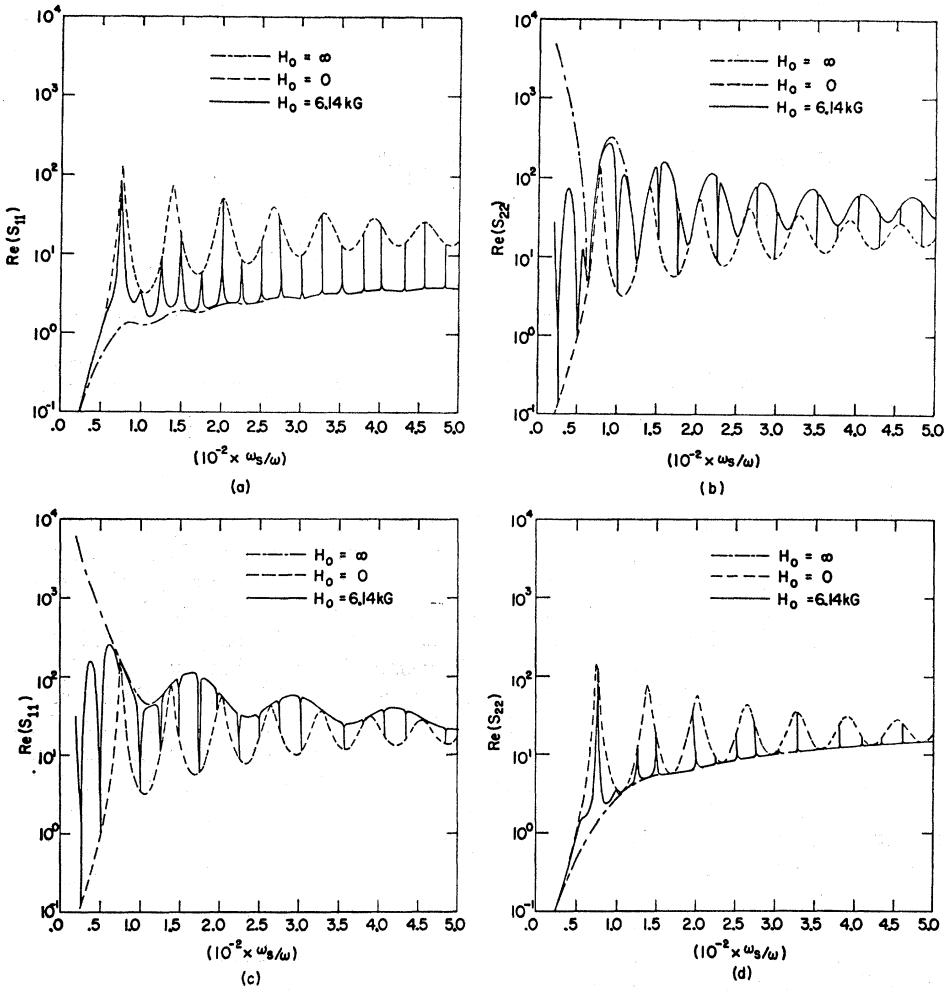

FIG. 17(a). The longitudinal sound wave attenuation results for open orbits undergoing magnetic breakdown in the case corresponding to Fig. 2, i.e., open orbit in real space parallel to **q**, where the oscillating probabilities mentioned in the text were used. The values of the parameters are $v_F/v_s = 500$, $ql = 40$, and $\beta = 8 \times 10^{-5}$; (b) the corresponding results for transverse waves; (c) the results for longitudinal waves in the case correspond to Fig. 3, $\theta = 0°$, i.e., open orbit in real space perpendicular to **q**; (d) the corresponding results for transverse waves.

ACKNOWLEDGMENTS

The author wishes to thank Professor L. M. Falicov for suggesting this problem and both Professor Falicov and Professor Morrel H. Cohen for much patience and many helpful discussions. Thanks go also to the systems staff at the University of Chicago Computation Center for much help in programming the problem for the IBM 7094-7040. The author is grateful to the Advanced Research Projects Agency and the National Science Foundation for direct financial support of this work. In addition, this research benefited from general support of related solid-state theory in the Institute for the Study of Metals by the U. S. Office of Naval Research and the National Aeronautics and Space Administration.

APPENDIX

In order to indicate how (2.24) and (2.25) were evaluated, the time in the lth Fermi surface piece is defined by

$$\omega t = \varphi - \varphi_{l,1}, \tag{A1}$$

where for $t = t_l$, $\varphi = \varphi_{l,2}$. The angle φ designates the electrons position on the Fermi surface. For example, in Fig. 1(a) the pieces of the Fermi surface are numbered so that $\varphi_{1,1} = \pi - \theta$, $\varphi_{1,2} = \pi + \theta$; $\varphi_{2,1} = \theta$, $\varphi_{2,2} = \pi - \theta$; etc. Solving (2.2) and (2.3) we have for any piece

$$v_1(\varphi) = (\hbar k_0/m)\cos\varphi, \quad v_2(\varphi) = (\hbar k_0/m)\sin\varphi, \tag{A2}$$

and since we always take $\mathbf{q} = q\hat{x}$, we have

$$\mathbf{q}\cdot\mathbf{r} = X\sin\varphi\ . \tag{A3}$$

The index l has been dropped as unnecessary, where **r** and **v** are expressed in terms of φ. We can eliminate the dimensioned constants by defining $\mathbf{V} = (m/\hbar k_0)\mathbf{v}$, and $\mathbf{\Pi}(l,\varphi) = (-\omega m/|e|\hbar k_0)\mathbf{J}(l,t)$.

In these terms, grouping factors, we obtain for (2.24)

$$\left(\frac{\sigma_e}{\sigma_0}\right)_{ij} = \frac{1}{\pi\omega\tau}\sum_{l=1}^{n}\int_{\varphi_{l,1}}^{\varphi_{l,2}} V_i(\varphi)\Pi_j(l,\varphi)\,d\varphi, \tag{A4}$$

where $\sigma_0 = N_0 e^2\tau/m$. We obtain **R** from (A4) and (2.28). We also have from (2.17)

$$\mathbf{\Pi}(l,\varphi) = \mathbf{\Xi}(l,\varphi) + D(l,\varphi)\sum_{p=1}^{n} B_{lp}\mathbf{\Pi}(p,\varphi_{p,2}), \tag{A5}$$

where

$$\begin{pmatrix}\Xi_1(l,\varphi)\\ \Xi_2(l,\varphi)\end{pmatrix} = g_1(\varphi,0)\lim_{\gamma'\to 0}\begin{bmatrix}\dfrac{-i}{X} & \dfrac{d}{d\gamma'}\\ -i\dfrac{d}{dX} & \end{bmatrix}\int_{\varphi_{l,1}}^{\varphi} g_2(\varphi',\gamma')d\varphi', \quad \text{(A6)}$$

$$g_1(\varphi,\gamma) = \exp[-iX\sin(\varphi+\gamma)+i(\omega_s/\omega)\varphi-\varphi/\omega\tau], \quad \text{(A7)}$$

$$g_2(\varphi',\gamma') = \exp[iX\sin(\varphi'+\gamma')-i(\omega_s/\omega)\varphi'+\varphi'/\omega\tau], \quad \text{(A8)}$$

and

$$D(l,\varphi)=\exp[iX(\sin\varphi_{l,1}-\sin\varphi)+i(\omega_s/\omega)(\varphi-\varphi_{l,1}) -(\varphi-\varphi_{l,1})/\omega\tau]. \quad \text{(A9)}$$

Using the well-known relation

$$\exp[iX\sin\varphi]=\sum_{m=-\infty}^{\infty} J_m(X)e^{im\varphi}, \quad \text{(A10)}$$

we have

$$g_1(\varphi,\gamma) = \sum_{m=-\infty}^{\infty} J_m(X)\exp\left[-im(\varphi+\gamma)+i\frac{\omega_s}{\omega}\varphi-\frac{\varphi}{\omega\tau}\right], \quad \text{(A11)}$$

$$g_2(\varphi',\gamma') \sum_{m=-\infty}^{\infty} J_m(X)\exp\left[im(\varphi'+\gamma')-i\frac{\omega_s}{\omega}\varphi'+\frac{\varphi'}{\omega\tau}\right].$$

With this it is readily apparent how the integrals in (A4) and (A6) can be carried out.

In performing the sums in (A4) each piece contributes a leading term which involves a double sum over products of Bessel functions. Considering the example (Fig. 1) of the sum of these terms over the Fermi surface yields terms of the form

$$\int_{-\theta}^{\theta} g_1\int_{-\theta}^{\varphi} g_2 d\varphi' d\varphi+\int_{\theta}^{\pi-\theta} g_1\int_{\theta}^{\varphi} g_2 d\varphi' d\varphi +\int_{\pi-\theta}^{\pi+\theta} g_1\int_{\pi-\theta}^{\varphi} g_2 d\varphi' d\varphi+\int_{\pi+\theta}^{2\pi-\theta} g_1\int_{\pi+\theta}^{\varphi} g_2 d\varphi' d\varphi, \quad \text{(A12)}$$

where the arguments are understood. These double sums can be eliminated by noting that (A12) can be expressed as

$$\int_{-\theta}^{2\pi-\theta} g_1\int_{-\theta}^{\varphi} g_2 d\varphi' d\varphi -\left[\int_{\theta}^{\pi-\theta} g_1 d\varphi+\int_{\pi-\theta}^{\pi+\theta} g_1 d\varphi+\int_{\pi+\theta}^{2\pi-\theta} g_1 d\varphi\right]\int_{-\theta}^{\theta} g_2 d\varphi' -\left[\int_{\pi-\theta}^{\pi+\theta} g_1 d\varphi+\int_{\pi+\theta}^{2\pi-\theta} g_1 d\varphi\right]\int_{\theta}^{\pi-\theta} g_2 d\varphi' -\left[\int_{\pi+\theta}^{2\pi-\theta} g_1 d\varphi\right]\int_{\pi-\theta}^{\pi+\theta} g_2 d\varphi', \quad \text{(A13)}$$

where using orthogonality properties of the exponentials in the first term, we are left with single sums and products of single sums. The sums were carried out with enough terms to ensure a minimum of five-place accuracy over the entire range of fields.

These remarks outline the nontrivial points of procedure. The rest is quite straightforward. The results were obtained numerically from the computer and are contained in the figures described in the main text.